Macromolecules

pubs.acs.org/Macromolecules Article

Role of Polymer–Nanoparticle Interactions on the Fracture Toughness of Polymer-Infiltrated Nanoparticle Films

Yiwei Qiang, Kevin T. Turner,* and Daeyeon Lee*

Cite This: *Macromolecules* 2023, 56, 122–135 Read Online

ACCESS | Metrics & More | Article Recommendations | Supporting Information

ABSTRACT: Polymer–nanoparticle (NP) composite films (PNCFs) with extremely high loadings of NPs (>50 vol %) have superb transport, thermal, and electrical properties. A new class of highly loaded PNCFs known as polymer-infiltrated NP films (PINFs) have been recently developed and applied as multifunctional coatings and membranes. PINFs also represent a powerful platform to study the interfacial and confinement effects on thermal, transport, and mechanical properties of polymers. In this work, we investigate the role of the polymer–NP interface on the fracture behavior of PINFs prepared by capillary rise infiltration of polymer into silica (SiO_2) NP packings. We tune the polymer–NP interaction strength by using SiO_2 NPs with two different surface functional groups (hydroxyl and trimethylsilyl) and two polymers [polystyrene and poly(2-vinyl-pyridine)] with different interaction strengths with SiO_2 NPs. For PINFs composed of small NPs, passivation of NPs with trimethylsilyl groups significantly impacts the fracture toughness by changing the sliding shear stress at polymer–NP interface. Polystyrene and poly(2-vinyl-pyridine) show a similar level of sliding shear stress likely due to strong adsorption on hydroxylated SiO_2 NPs. In contrast, for PINFs consisting of large NPs, the fracture toughness is more strongly affected by the fracture properties of the polymers than the polymer–NP interactions. Our results illustrate the importance of understanding the interplay between confinement and polymer–NP interactions in controlling and tuning the fracture properties of PINFs for a wide range of applications.

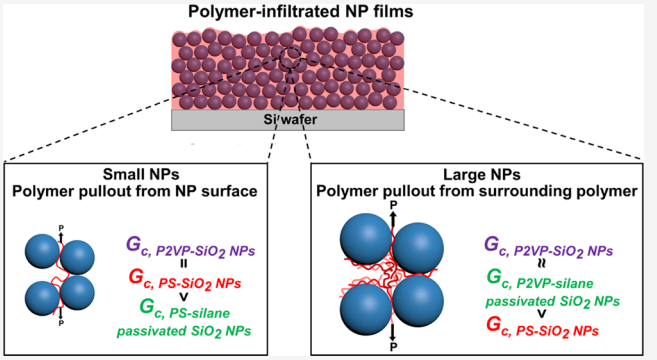

1. INTRODUCTION

Polymer–nanoparticle (NP) composite films (PNCFs) have attracted significant scientific and technological interest due to synergistic combination of the functionality of NPs and the flexibility and processibility of polymers.[1−3] PNCFs with an extremely high filler content (>50 vol %) have shown superior transport, thermal, and electrical properties compared to their counterparts with a low filler content.[4,5] For example, composite separation membranes with a large fraction of NPs overcome the trade-off between permeability and selectivity in many traditional polymer membranes.[6,7] PNCFs containing high concentrations of conductive NPs exhibiting thermal or electrical conductivity orders of magnitude larger than PNCFs with low concentrations of NPs.[8,9]

One defining feature in PNCFs is that the surface-to-volume ratio of NPs increases dramatically compared to conventional composites with microparticles, magnifying the importance of polymer–NP interfacial interactions.[2] For example, stiffening and strengthening of PNCFs generally rely on strong interfaces that facilitate effective stress transfer, while toughening may benefit from weak interfaces due to crack deflection.[4,10−12] Interfacial interactions also impact gas, thermal, and charge transport across the interfaces and ultimately the macroscopic properties of PNCFs.[3,13,14] Such a dependence is especially true for highly loaded PNCFs with an extremely large interfacial area. Another important consequence of having high loadings of NPs in PNCFs is that the interparticle distance can be comparable to or even smaller than the characteristic size of the polymers in their unperturbed state. Such confinement alters various physical properties of polymers, such as dynamics,[15,16] thermal conductivity,[17] viscosity,[18] and permeabiliy,[19] from the bulk values. The mechanical properties of confined polymers, including elastic modulus, strength, and toughness, are also known to drastically deviate from the bulk[20−22] and thus understanding such deviation is essential for practical use of highly loaded PNCFs.

Compared to studies on the mechanical properties of neat polymer thin films and PNCFs with low filler content,[20,23,24] there are relatively few studies on PNCFs with high filler content, with most of them focusing on stiffness and

Received: July 28, 2022
Revised: October 24, 2022
Published: December 21, 2022

https://doi.org/10.1021/acs.macromol.2c01567
Macromolecules 2023, 56, 122−135

strength.[21,22,25−27] The fracture toughness of highly loaded PNCFs, a material property that quantifies the material's resistance to crack propagation,[28] is difficult to predict and understand due to complexity associated with their structures, challenges in fabricating such PNCFs using conventional methods,[4,29] and limited testing methods available for these materials.[23] It is even more challenging to distinguish the role of interfacial interactions from the confinement effect, as they are often convoluted and difficult to decouple.[21,30,31] In addition, varying interfacial interactions often change the dispersion state of NPs in PNCFs and thus the extent of confinement experienced by polymers, complicating data interpretation.[32,33]

A new class of highly loaded PNCFs that circumvents many of fabrication challenges is polymer-infiltrated NP films (PINFs) prepared based on capillarity-based phenomena.[29,34−36] In capillary rise infiltration (CaRI), a bilayer film composed of a densely packed NP layer and a polymer layer is thermally annealed above the glass transition temperature (T_g) of the polymer to induce polymer wicking into the interstices between the NPs via capillarity.[34] Alternatively, infiltration can be achieved at room temperature (RT) using solvent-driven infiltration of polymer (SIP), which takes advantage of capillary condensation.[35,37] CaRI and SIP processes are robust methods of producing PINFs with a wide range of polymers and NPs, enabling the fabrication of multifunctional coatings and membranes for various applications.[29,38,39]

In addition to being potentially scalable methods to fabricate highly loaded PNCFs, CaRI and SIP provide a robust platform to systematically study the effect of confinement and polymer−NP interactions on the mechanical, thermal, and transport properties of polymers.[30,31,40−42] Given that the average pore radius (R_{pore}) in a random close-packed spherical NPs (~65 vol %) is ~29% of the particle radius, the extent of confinement imposed on the polymer chains can be readily tuned by changing NP size and/or the molecular weight (M_W) of the polymer. By changing the type of polymer used in CaRI while keeping NP size and polymer MW constant, interfacial effects can be systematically studied. A recent study shows that under extreme confinement, polymers in PINFs with stronger polymer−NP interaction strength show slower segmental dynamics with larger gradient.[43] Polymer−NP interaction strength also strongly affects the dynamics of the SIP process based on experimental and simulation results.[35,44] Recently, we investigated the effect of confinement on the fracture behavior of PINFs with weakly attractive interactions composed of dense packings of SiO_2 NPs infiltrated with a glassy polymer, polystyrene (PS).[45] We showed that the polymers can toughen NP films dramatically through a confinement-induced molecular bridging mechanism when they are under extreme confinement and completely lose interchain entanglement. As the confinement ratio (CR) decreases, the bridging mechanism becomes less pronounced, and polymer interchain entanglement becomes the main toughening mechanism. While this prior study sheds light on the role of polymer bridging and entanglement on the fracture toughness of PINFs, significantly less is known about the role of interactions between NPs and polymers on the fracture toughness.

In this work, we investigate the effect of polymer−NP interactions on the fracture behavior of PINFs. We tune the polymer−NP interaction strength by using SiO_2 NPs with two different surface functional groups (hydroxyl and trimethylsilyl) and two polymers that are known to have different interaction strengths with SiO_2 NPs, despite having similar structures [PS and poly(2-vinyl-pyridine) (P2VP)].[31] We show that the interplay between interfacial shear stress between NPs and polymer and the intrinsic properties of the polymer influence the toughness of these PINFs. Our results offer insights into the effect of polymer−NP interactions on the fracture behavior of confined polymers and provide important guidelines for the scalable manufacturing of damage-tolerant PINFs.

2. MATERIALS AND METHODS

2.1. Materials. Polystyrene (PS) (2 k PS, M_n = 2000 g mol^{-1}, PDI = 1.09; 8 k PS, M_n = 8000 g mol^{-1}, PDI = 1.10; 21 k PS, M_n = 21,000 g mol^{-1}, PDI = 1.04; 51 k PS, M_n = 51,000 g mol^{-1}, PDI = 1.03; 158 k PS, M_n = 158,000 g mol^{-1}, PDI = 1.06; 173 k PS, M_n = 173,000 g mol^{-1}, PDI = 1.06; 498 k PS, M_n = 498,000 g mol^{-1}, PDI = 1.09; 1 M PS, M_n = 1,000,000 g mol^{-1}, PDI = 1.05; 2.1 M PS, M_n = 2,100,000 g mol^{-1}, PDI = 1.15; 4 M PS, M_n = 4,049,000 g mol^{-1}, PDI = 1.09), poly(2-vinyl pyridine) (P2VP) (2 k P2VP, M_n = 2000 g mol^{-1}, PDI = 1.20; 8 k P2VP, M_n = 7800 g mol^{-1}, PDI = 1.08; 22 k P2VP, M_n = 22,000 g mol^{-1}, PDI = 1.06; 50 k P2VP, M_n = 50,000 g mol^{-1}, PDI = 1.08; 67 k P2VP, M_n = 67,000 g mol^{-1}, PDI = 1.07; 121 k P2VP, M_n = 121,000 g mol^{-1}, PDI = 1.07; 190 k P2VP, M_n = 190,000 g mol^{-1}, PDI = 1.25; 900 k P2VP, M_n = 900,000 g mol^{-1}, PDI = 1.5) and atactic (hetero >50%) polymer methyl methacrylate (7 k PMMA, M_n = 7000 g mol^{-1}, PDI = 1.19, 21 k PMMA, M_n = 20,500 g mol^{-1}, PDI = 1.14; 45 k PMMA, M_n = 45,000 g mol^{-1}, PDI = 1.10; 99 k PMMA, M_n = 99,000 g mol^{-1}, PDI = 1.12) are purchased from Polymer Source, Inc. 152 k P2VP (M_n = 152,000 g mol^{-1}, PDI = 1.05), trimethylchlorosilane (TMCS, ≥98.0% (GC)) and silica (SiO_2) NPs with diameters of 9 nm (LUDOX SM-30, 30 wt % suspension in water)) and 27 nm (LUDOX TM-50, 50 wt % suspension in water) are purchased from Sigma-Aldrich. SiO_2 NPs with diameters of 79 nm (SNOWTEX ST-YL, 40−41 wt % suspension in water) and 100 nm (SNOWTEX ST-ZL, 40−41 wt % suspension in water) are obtained from Nissan Chemical America Corp.

2.2. Preparation of PINFs. PINFs are prepared as previously described.[45] Prior to film deposition, single-side-polished 4-inch Si wafers (100) with a 1 nm native oxide layer (University Wafer) are rinsed with isopropanol and deionized water, dried with nitrogen, and then treated by oxygen plasma for ~4 min. To avoid crack formation during polymer infiltration, a polymer-top geometry is used, where the NP film is spin-coated first, followed by the polymer film.[30] The SiO_2 NP suspensions are diluted with deionized H_2O and filtered prior to use (filter pore size 0.45 μm). The filtered NP suspensions are spin-coated onto cleaned Si wafers using a WS-400BZ-6NPP/Lite spin coater (Laurell Technologies Corporation). The concentration of NP suspensions and spin-coating rate are controlled to form a densely packed NP film with a thickness of ~250 nm. Then, a solution of PS dissolved in toluene or P2VP dissolved in butanol is spin-coated onto the NP film to form a bilayer film. The bilayer film is heated at 180 °C (except for P2VP infiltration into 9 and 27 nm NP packings where higher temperature is needed for infiltration) in a nitrogen-filled oven for 3 h to allow infiltration of the polymer into the pores of the NP packing. Since the pores can be partially infiltrated with polymers during spin coating, the concentration of polymer solutions and spin-coating rate are carefully controlled, such that the pores are close to be completely filled after thermal annealing and there is no residual polymer layer atop the PINF. Silane-passivated SiO_2 NP films are prepared by exposing SiO_2 NP films to TMCS vapor in a deposition chamber at RT for overnight before polymer deposition and infiltration. PS (2, 8, 21, 51 k) and P2VP (2, 8, 22, 50 k) films with thicknesses of ~200 nm are prepared to obtain fracture toughness of neat polymers. 50 nm 173 k PS/152 k P2VP and 200 nm 158 k PS/152 k P2VP films are also deposited on plasma-treated or silane-passivated Si wafers and annealed at 180 °C for 3 hrs for polymer-SiO_2 adhesion measurements.

https://doi.org/10.1021/acs.macromol.2c01567
Macromolecules 2023, 56, 122−135

2.3. Glass Transition Temperature Measurements. The glass transition temperature (T_g) of the polymer confined in NP packings is measured using a J.A. Woollam M-2000V spectroscopic ellipsometer as previously described.[30,31,41,43,46] A bilayer film composed of a polymer layer atop a PINF is mounted onto a temperature-controlled stage (Linkam THMS 600) that is attached to the ellipsometer and enclosed in a nitrogen-filled chamber. The in situ ellipsometry sampling rate is 1 s with high accuracy zone-averaging. Three heating and cooling cycles are performed on each sample, with a heating rate of 90 K/min and a cooling rate of 10 K/min. In each cycle, the sample is heated from 303 K to the target temperature (ranging from 423 to 503 K depending on polymer MW and particle size) and then cooled to 303 K. T_g data are measured from the cooling cycles. The thickness and refractive indices of the polymer layer and the PINF are determined by fitting the cooling ramp raw data to the Cauchy model. T_g of the confined polymer is determined via the intersection of the linear fits to the melt and glassy regimes in the plots of refractive index of PINF versus temperature. The thickness of the PINF is held constant during the dynamic data fits. The bulk polymer T_g is determined using the same protocol on the refractive index of the top polymer layer versus temperature. The polymer layer is at least 100 nm thick, such that the measured T_g would be close to the bulk value.

2.4. Fabrication of Double Cantilever Beam Specimens. The double cantilever beam (DCB) specimens are prepared by first constructing a sandwich structure composed of Si/epoxy/metal/testing film/Si, as depicted in Figure 4a. All PINFs have thicknesses of ~250 nm. For PS and P2VP-infiltrated NP films, a metal layer consisting of 25 nm thick Ti and 100 nm thick Al layer is deposited on the testing films by magnetron sputtering (Denton Explorer-14). For PMMA-infiltrated NP films, a 20 nm layer of Al_2O_3 is deposited by atomic layer deposition (Cambridge NanoTech S200 ALD) on the testing films before Ti and Al deposition (see Supporting Information for detailed discussion). The metal/metal compound layer acts as a barrier layer to prevent the permeation of epoxy into testing films as well as a stiff elastic standoff layer to prevent plastic deformation of epoxy and associated energy contribution to the fracture toughness of testing films. Afterward, epoxy adhesives (EPO-TEK 353ND, Epoxy Technology, MA) with ~5 μm thickness are spin-coated onto the metal layer and a dummy Si wafer is attached for making the sandwich structure. The sandwich structure is then diced with a dicing saw (ADT 7100 Dicing Saw) to create 10 mm wide DCB specimens. To quantify polymer-SiO_2 adhesion, asymmetric DCB (ADCB) specimens are fabricated similarly, except that polymers are deposited on 375 μm thick wafers and bonded with 500 μm thick wafers. In addition, a 50 nm Au layer is deposited on part of the films before Ti deposition to create a weak interface and facilitate crack initiation.

2.5. DCB Fracture Testing. Fracture testing of the DCB specimens is conducted using a MTS test system (Criterion Model 43) fitted with a 50 N load cell. Two loading blocks are attached to the ends of the specimen and the specimen is loaded in at a constant displacement rate of 1 mm min^{-1}. When stable crack propagation is observed, the specimen is unloaded and then reloaded. Multiple loading/crack-growth/ unloading cycles are performed until complete fracture of the specimen and the load–displacement curves are obtained. The crack length, a, is calculated based on the compliance of the specimen using[47]

$$a = \left(\frac{CE'Bh^3}{8}\right)^{1/3} - 0.64h \tag{1}$$

where the compliance, C, is the inverse slope of the load–displacement curve corrected for machine compliance, E' is the plane-strain modulus of the beam, B is the specimen width, and h is the height of one beam. The critical load, P_c, at which crack growth occurs, is the load at which the slope of the load–displacement curve begins to decrease during the loading cycle. The fracture toughness of the film, G_c, which is the critical value of applied strain energy release rate, can be calculated by substituting a and P_c into eq 2:

$$G_c = \frac{12P_c^2a^2}{E'B^2h^3}\left(1 + 0.64\frac{h}{a}\right)^2 \tag{2}$$

For ADCB specimens, a and G_c are calculated based on eqs 345, respectively.[48,49]

$$a = (3CE'I)^{1/3} - 0.64I\left(\frac{12}{bh_1^2} + \frac{12}{bh_2^2}\right) \tag{3}$$

$$G_c = \frac{6P_c^2}{E'B^2}\left[\left(\frac{a}{h_1} + 0.64\right)^2\frac{1}{h_1} + \left(\frac{a}{h_2} + 0.64\right)^2\frac{1}{h_2}\right] \tag{4}$$

$$I = \left(\frac{12}{bh_1^3} + \frac{12}{bh_2^3}\right)^{-1} \tag{5}$$

where h_1 and h_2 are the thicknesses of the top and bottom beams, respectively.

Multiple values of G_c are obtained for each specimen and at least three specimens are measured for each sample. Two or more samples are measured for most conditions and the G_c reported is the average G_c of all specimens with the same condition. We observe consistent data at different crack lengths of a specimen, between different specimens of a sample or across different samples. The fractured surface of each specimen is checked carefully, and any data point associated with adhesive fracture is discarded.

2.6. Nanoindentation of Neat NP Films and PINFs. The modulus of neat NP films and PS-infiltrated NP films (>600 nm in thickness) is measured using a Hysitron TI 950 TriboIndenter. A diamond Berkovich tip is used and the area function of the tip is calibrated through a series of indents on a fused quartz standard sample. Before all measurements, the thermal drift is stabilized to less than 0.3 nm s^{-1}. For each sample, 16 indentation tests, with 9 partial unloading cycles each, are performed on a 4 × 4 grid with a spacing of 10 μm between the indents. The maximum loads in the test range from 100 to 300 μN, resulting in indentation depths from 20 to 70 nm. The modulus of films is determined from the load–displacement curves following the Oliver-Pharr method[50] using a Triboscan software. Tests with indentation depths <10% of film thickness are used for analysis as the area function is well calibrated in this range and the substrate effect is negligible.

2.7. Characterization of Silane-Passivated Surfaces. Untreated and silane-passivated SiO_2 NP films are exposed to saturated water vapor using a vapor annealing chamber setup previously described,[35,37] and in situ spectroscopic ellipsometry (SE) measurements (Alpha-SE, J.A. Woollam) are performed to monitor the refractive index changes of these films. To obtain the surface area and pore size distribution of SiO_2 NP packings before and after silane passivation, bulk SiO_2 NP packings are prepared by drying SiO_2 NP suspensions at 80 °C in an oven for overnight and using the same silane treatment conditions as thin films. Nitrogen adsorption–desorption measurements are conducted on these bulk samples using a Micromeritics Tristar II surface area and porosity analyzer at the liquid nitrogen temperature. Before the measurements, the samples are degassed overnight under vacuum. The surface energies of untreated and silane-passivated SiO_2 surfaces are obtained by measuring the static contact angle of water and diiodomethane on plasma-treated and silane-passivated Si wafers using a goniometer (Biolin Scientific Attension) and analyzing with the Owens–Wendt model (see Supporting Information). It is assumed that the surface properties of plasma-treated and silane-passivated Si wafers are similar to those of the as-prepared and silane-passivated SiO_2 NPs.

2.8. Characterization of PINFs and Neat Polymer Films. The thicknesses and refractive indices of the as-prepared PINFs are measured using SE and the polymer volume fractions are calculated as previously described.[30] The thicknesses and refractive indices of the fractured films are also measured and compared with the as-prepared films to determine the location of the crack path.[45] The surface morphologies of the as-prepared and fractured films are imaged using

https://doi.org/10.1021/acs.macromol.2c01567
Macromolecules 2023, 56, 122–135

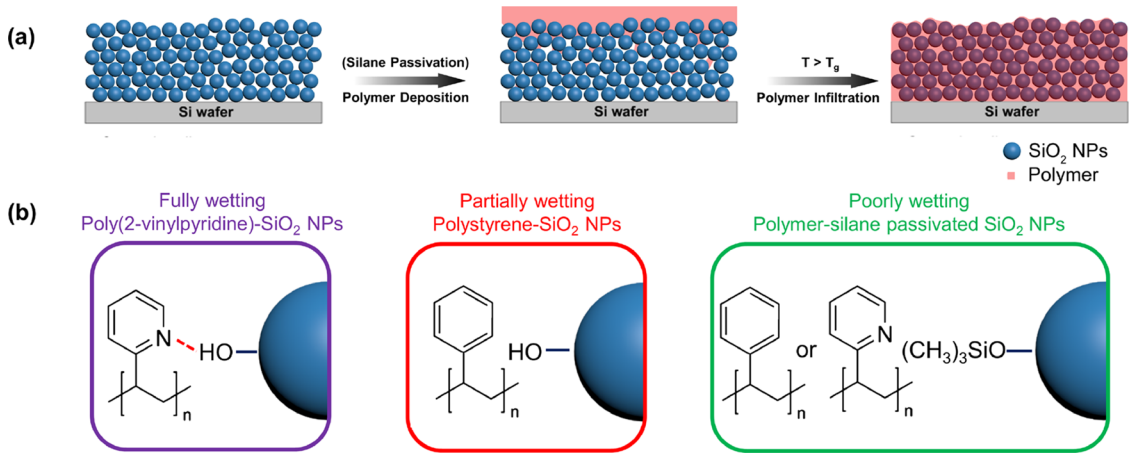

Figure 1. Preparation of PINFs with different polymer−NP Interaction strengths: (a) Schematic showing the preparation of a PINF by depositing a polymer atop a densely packed NP layer and infiltrating polymer into the voids of the NP layer via capillarity. Silane passivation is performed on some of the NP films before polymer deposition. (b) Schematic showing the polymer−NP systems with three different wetting conditions used in this study.

a scanning electron microscope (FEI-600 Quanta ESEM). Before imaging, each sample is coated with 4 nm of iridium to prevent charging. The scanning electron microscopy (SEM) images are captured at an accelerating voltage of 20 kV, a spot size of 3.0, and working distance around 10 mm. Atomic force microscopy (AFM) images of fractured polymer films are collected using a Bruker Dimension Icon AFM with a silicon tapping-mode probe. Gwyddion software is used to process the images and extract the root-mean-square roughness.

3. RESULTS AND DISCUSSION

3.1. Tuning Polymer−NP Interaction Strength. We prepare PINFs by first fabricating a bilayer film composed of a polymer layer atop a densely packed SiO_2 NP layer (packing fraction ∼65 vol %) and subsequently heating the bilayer above the glass transition temperature (T_g) of the polymer to induce its wicking into the interstices of the NP packing (Figure 1a). To investigate the role of the polymer−NP interface on the fracture behavior of PINFs, we tune polymer−NP interaction strength by varying the type of polymer used or changing the surface chemistry of NPs (Figure 1b). In our previous work, we focus on a partially wetting system: poly(styrene) (PS)-SiO_2 NPs where contact angles ranging from 7 to 23° have been reported for PS on the SiO_2 surface.[45,51,52] In this work, to increase the interaction strength, we use P2VP, which is a polymer with a similar structure as PS but has a nitrogen atom capable of forming strong hydrogen bonding with the hydroxyl groups on the SiO_2 NPs and thus fully wet the surface.[31,53−55] To decrease the interaction strength, we passivate the SiO_2 NPs with trimethylsilyl groups before polymer deposition and infiltration. To quantitatively compare the interaction strength between these systems, we estimate the thermodynamic work of adhesion between the polymer and SiO_2 NPs ($W_{polymer-NP}$) based on eq 6.[32,56,57]

$$W_{polymer-NP} = 2 \times \left(\sqrt{\gamma_P^d \gamma_{NP}^d} + \sqrt{\gamma_P^p \gamma_{NP}^p}\right) \quad (6)$$

where γ_{NP}^d and γ_{NP}^p are the dispersive and polar components of NP surface energies, respectively; γ_p^d and γ_{NP}^p are the dispersive and polar components of polymer surface energies, respectively (Table S1). As shown in Table 1, P2VP-SiO_2 has a $W_{polymer-NP}$ of 113.8 mJ/m^2, larger than that of PS-SiO_2 (91.5 mJ/m^2). In the case of silane-passivated SiO_2 NPs, $W_{polymer-NP}$ decreases significantly for both polymers.

Table 1. Estimated Work of Adhesion between the Polymer and SiO_2 NPs

polymer	SiO_2 NPs	thermodynamic work of adhesion $W_{polymer-NP}$ (mJ/m^2)
polystyrene	untreated	91.5
poly(2-vinylpyridine)	untreated	113.8
polystyrene	silane-passivated	66.1
poly(2-vinylpyridine)	silane-passivated	76.4

Water contact angle and ellipsometry measurements are performed to characterize untreated and silane-passivated SiO_2 NP films (Figure 2a). Plasma-cleaned Si wafers with a thin native SiO_2 layer are also characterized for comparison. Due to the presence of abundant surface hydroxyl groups, untreated NP films and Si wafers are hydrophilic with water contact angles lower than 5°. After silane passivation, the water contact angle increases to 90 ± 4° for Si wafers and above 90° for NP films. The difference between smooth Si wafers and NP films and the trend of increasing contact angle with NP diameter can be attributed to the increase in surface roughness.[58] Ellipsometry measurements show that the porosity of untreated NP films is similar (∼0.35) but shows a non-monotonic trend after silane treatment. The maximum lateral extension of a trimethylsilyl group is reported to be ∼0.37 nm,[59,60] and such passivation has been reported to decrease the pore diameter of mesoporous silica up to 0.65 nm.[61] Given that the average pore radius (R_{pore}) in a disordered packing of spherical NPs is approximately 29% of the particle radius,[62] R_{pore} increases from 1.2 to 14.5 nm, as NP size increases from 9 to 100 nm (Table S2). Due to the significantly larger size of the pores compared to size of trimethylsilyl groups, the porosity of 79 and 100 nm SiO_2 NP packings remains almost unchanged. The porosity shows a decrease of 0.037 in 27 nm NP packings, confirming successful passivation of NPs. Although a larger porosity decrease is expected in 9 nm NP packings, only a slight decrease of 0.01 is observed, indicating inefficient passivation likely due to strong steric hindrance. In-situ ellipsometry measurements of SiO_2 NP films exposed to

https://doi.org/10.1021/acs.macromol.2c01567
Macromolecules 2023, 56, 122−135

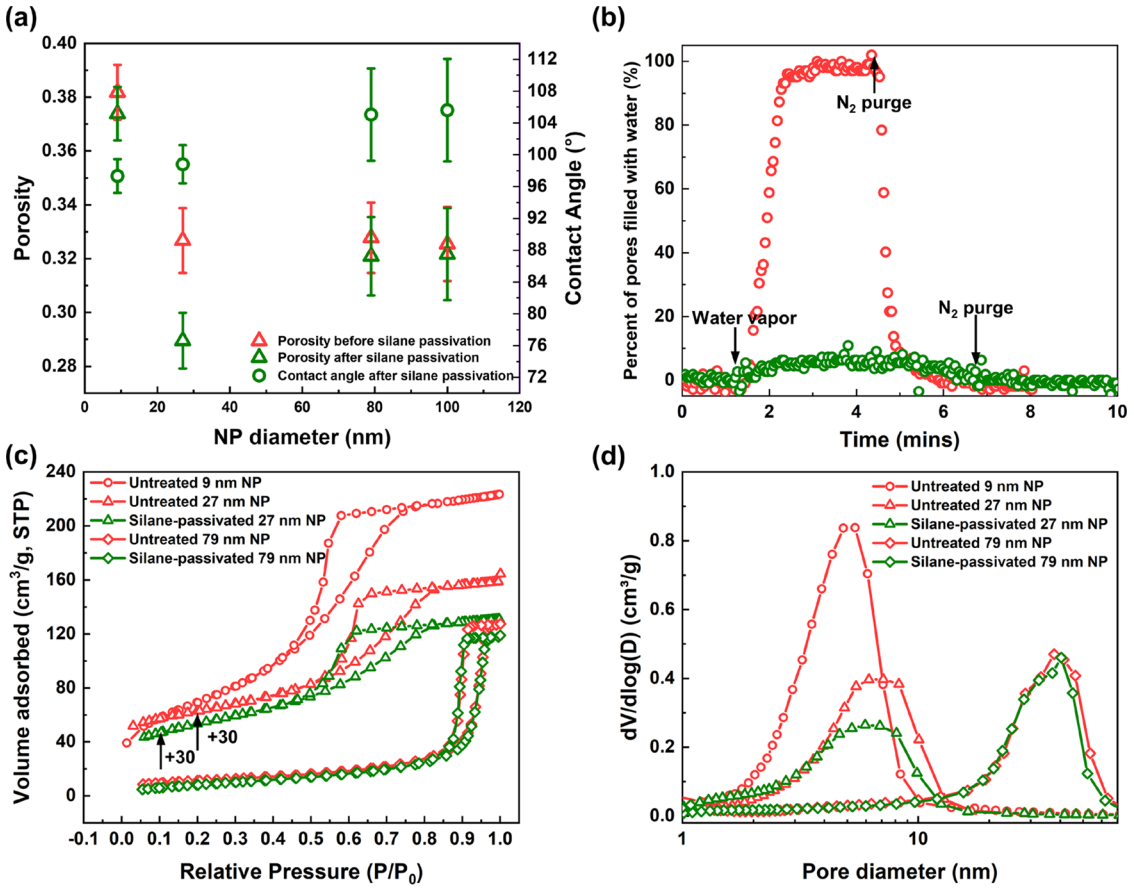

Figure 2. Characterization of NP films: (a) Porosity in SiO_2 NP films before and after silane passivation (left axis) and contact angle of water on silane-passivated SiO_2 NP films (right axis). (b) Percent of pores filled with condensed water for untreated (red) and silane-passivated (green) 27 nm SiO_2 NP packings upon exposure to water vapor. (c) Nitrogen sorption isotherms and (d) pore size distribution of untreated and silane-passivated bulk SiO_2 NP packings with different NP diameters. The isotherms of 27 nm NP packings have been shifted upward by 30 cm^3/g for the sake of readability.

saturated water vapor further confirm the hydrophilic nature of untreated NPs with all voids being flooded with condensed water, whereas less than 10% of voids filled with water in the silane-passivated NP packings (Figures 2b and S1).[61] The small amount of water adsorbed in silane-passivated NP films may be attributed to the presence of residual hydroxyl groups as degassing of the samples before silanization is performed at RT. Elevated degassing temperature may increase silane coverage but can also lead to sintering between SiO_2 NPs and affect the toughness of PINFs.[61,63] Nevertheless, the silane treatment in this study is expected to significantly decrease polymer−NP interaction strength indicated by the dewetting of polymers on silane-passivated NP films (Figure S2) and faster polymer infiltration into silane-passivated NP films (Figure S3).

3.2. Effect of Polymer−NP Interaction Strength on Polymer Segmental Dynamics. While this paper focuses on the fracture behavior of PINFs, we also measure the T_g of the polymer in PINFs which provides information on polymer segmental relaxation and is often affected by interfacial interactions.[64] Spectroscopic ellipsometry measurements on bilayer films composed of a fully infiltrated PINF with a neat polymer layer on top are performed as previously described.[30,46] The T_g values of the confined polymer in NP packings are determined based on refractive index change of the PINF layer with temperature on a controlled cooling ramp and compared to the bulk T_g values measured using the polymer layer atop the PINF (Figure S4). To estimate the degree of confinement, we define a CR as the ratio between the radius of gyration of the unperturbed polymer chain (R_g) to average pore radius (i.e., CR = R_g/R_{pore}).[45] Our previous studies have shown that stronger interactions between polymer and NP as well as stronger confinement lead to a greater positive shift in T_g (i.e., $\Delta T_g = T_{g,confined} - T_{g,bulk}$ is positive) of the polymer in PINFs.[30,31,41,43,46] As shown in Figure 3, confined polymers exhibit higher-than-bulk T_g for all the samples investigated. Even in silane-passivated 27 nm NP films, ΔT_g of PS increases with polymer MW (or CR) and reaches up to 28 K. Such an increase in T_g has been attributed to the loss of configurational entropy due to large geometrical confinement imposed on the polymer chains by the NPs.[31,41,65] In untreated 27 nm NP packings, a 45 K increase in the T_g of PS is observed due to stronger polymer−NP interactions. Similarly, while bulk P2VP and PS have almost the same T_g, larger increase in T_g up to 72 K is observed for confined P2VP because of the strong hydrogen bonding between the nitrogen atom in P2VP and the hydroxyl groups on the SiO_2 NP surface. A further segmental slowdown (larger ΔT_g) and larger difference in ΔT_g between PS and P2VP samples are observed in 9 nm NP packings relative to 27 nm NP packings. In the CR range of 5−8, the increase in T_g for 900 k P2VP (CR = 6.6) in 27 nm NP packing is 63 K, whereas

https://doi.org/10.1021/acs.macromol.2c01567
Macromolecules 2023, 56, 122−135

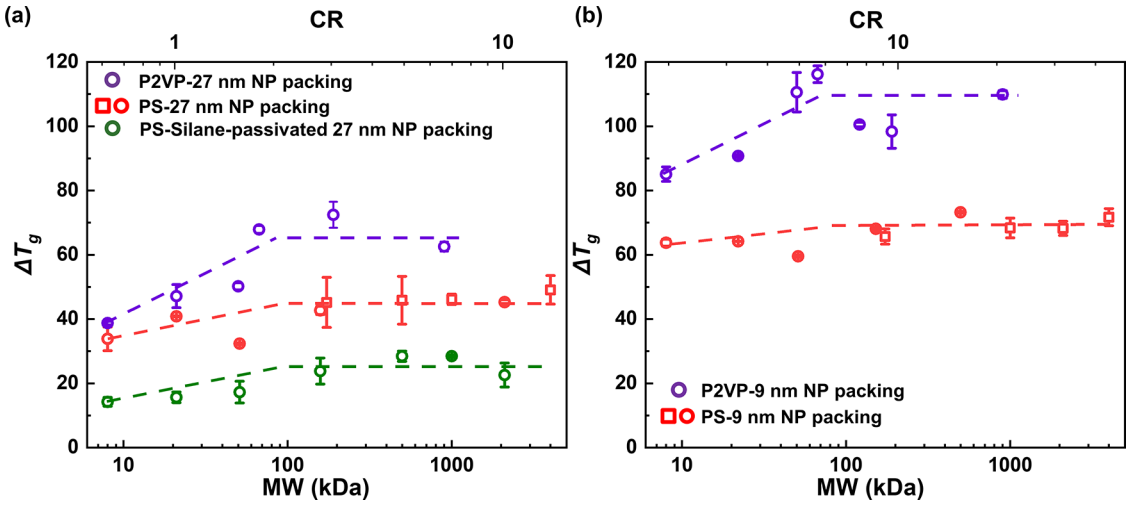

Figure 3. Segmental dynamics of polymers in PINFs: ΔT_g ($T_{g,confined} - T_{g,bulk}$) as a function of polymer MW and CR for PINFs made of PS/P2VP and (a) 27 nm NPs and (b) 9 nm NPs obtained in this study (circular symbols) and from reference (square symbols).[46] The lines are to guide the eye.

the increase in T_g for 67 k P2VP (CR = 5.7) and 121 k P2VP (CR = 7.6) in 9 nm NP packings is 116 and 100 K, respectively. This indicates that an unprecedented increase in T_g arises from the synergistic effects of extremely high level of geometric confinement in NP packings with unique concave pores and large interfacial area between SiO_2 and polymer. Overall, these results show that both confinement and polymer−NP interactions play important roles in polymer segmental dynamics.

3.3. Effect of Polymer−NP Interaction Strength on the Fracture Toughness of PINFs. As shown in our previous work,[45] the fracture behavior of PINFs is strongly affected by the degree of confinement. To focus on the effect of polymer−NP interaction strength, we keep CR unchanged by selecting P2VP with a similar MW as PS and choosing NP packings with approximately the same pore size after silane passivation. In addition, the dominant toughening mechanism in PINFs transitions from confinement-induced molecular bridging (9 and 27 nm) to polymer entanglement (79 and 100 nm) as NP size increases as discussed in our previous work.[45] Thus, PINFs with 9, 27, and 79 nm NPs are selected as the samples of interest for this study. The pore size decreases by <10% in 27 nm NP packings and remains almost unchanged in 79 nm NP packings after silane passivation based on nitrogen adsorption−desorption measurements performed on bulk SiO_2 NP packings (Figure 2c,d and Table S2).

3.3.1. PINFs with 9 and 27 nm NPs. To probe the fracture behavior of PINFs, we use a thin-film fracture testing method based on the DCB specimen as previously described.[45] A DCB specimen is fabricated by constructing a multilayer stack composed of Si/epoxy/metal/PINF/Si. The two Si beams are pulled apart at one end under a constant displacement rate, and the load−displacement (P-Δ) data are continuously recorded as illustrated in Figure 4a. Each specimen is initially loaded elastically, but once the strain energy release rate (G) exceeds the critical strain energy release rate (i.e., toughness G_c) of the PINF, a crack propagates in the PINF (Figures S5, S6, and S7). After extension of the crack by several millimeters, the specimen is unloaded and then subjected to multiple loading/crack-growth/unloading cycles until complete fracture to obtain multiple values of G_c from a single specimen. Figure 4b shows typical load−displacement curves from a DCB test on a PINF made of 21 k PS and untreated (red) and silane-passivated (green) 27 nm NPs. G_c at different crack lengths can be calculated using a compliance-based method (see Methods for detailed information). As G_c is proportional to the critical load squared (P_c^2), lower P_c at a similar crack length (e.g., the fifth cycle where compliances of the beams are similar) in silane-passivated NP packings compared to untreated packings corresponds to smaller G_c. As shown in Figure 4c, G_c of PINFs made of untreated and silane-passivated 27 nm NPs shows similar MW dependence, where G_c increases with MW before reaching a plateau at high MW. However, lower G_c values are observed with silane-passivated NPs at all MWs.

As described in our previous work, the dominant toughening mechanism for PINFs composed of 27 nm NPs is confinement-induced molecular bridging.[45] In this mechanism, the crack tip is bridged by many individual polymer chains strongly confined in the pores and the crack growth is resisted by the frictional pullout of chains that bridge the crack (Figure 4d).[60,66] Additional energy is dissipated by elongation of the bridging chains during the pullout process. The energy dissipated by chain pullout and elongation is predicted to be proportional to square of the maximum pullout length (δ_0), which is related to polymer MW (see Supporting Information for a detailed description). However, the bridging force also increases with polymer MW and eventually exceeds the strength of the polymer backbone, limiting δ_0 and thus G_c. G_c of composites toughened by this mechanism is given by the following expression[60]

$$G_c = G_0 + \frac{2f\tau}{d_{pore}}\left[\frac{1}{4}a^2 N \mathrm{erfc}\left(\frac{a\sqrt{N}}{2\sqrt{2}\,c}\right) - \frac{ca\sqrt{N}}{\sqrt{2\pi}}e^{-a^2N/8c^2} + c^2\mathrm{erf}\left(\frac{a\sqrt{N}}{2\sqrt{2}\,c}\right)\right](1+\varepsilon_{max}) \quad (7)$$

where G_o is fracture toughness of an unfilled matrix (0.4 J/m^2 based on measurements of untreated and silane-passivated 27 nm NP packings), f is the area density of the polymeric phase in the crack plane, τ is the sliding shear stress at the polymer−matrix interface, d_{pore} is the pore diameter, a is the Kuhn length

https://doi.org/10.1021/acs.macromol.2c01567
Macromolecules 2023, 56, 122−135

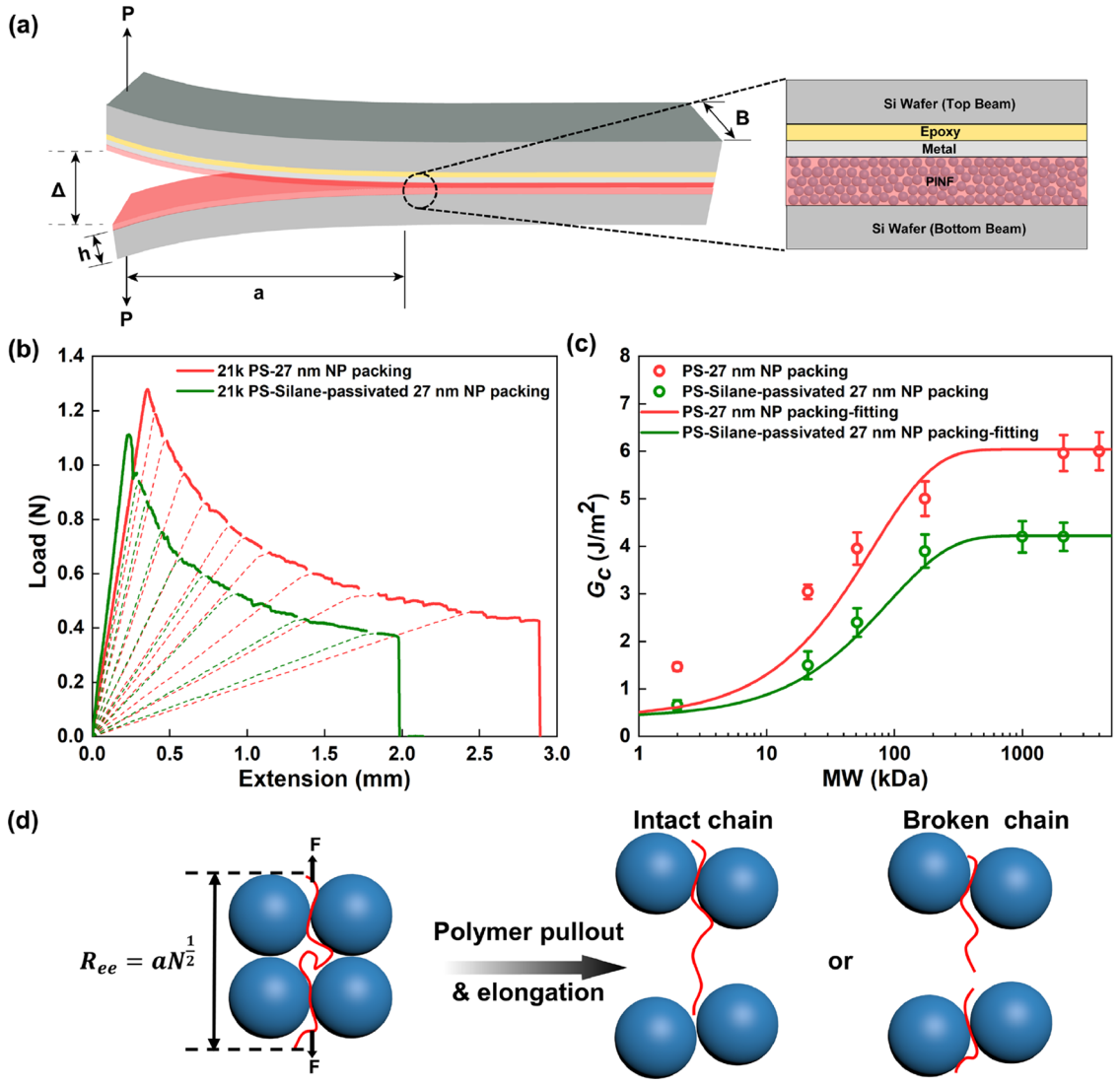

Figure 4. DCB fracture testing of PINFs and confinement-induced molecular bridging model: (a) Schematic of the DCB specimen used to measure the fracture toughness of PINFs. The relative thicknesses of each layer are not drawn to scale. (b) Representative load−displacement curves for a DCB test of PINFs made of 21 k PS and untreated (red) and silane-passivated (green) 27 nm NPs. Multiple loading/crack-growth/unloading cycles are performed on each specimen. The loading curves after the first cycles are plotted as dashed lines for better readability. (c) G_c as a function of polymer MW for PINFs made of PS and untreated/silane-passivated 27 nm NPs. The solid curves are fits of the data with the molecular strength-limited bridging model (eq 7). (d) Schematic illustration of a confined polymer chain that bridges the surrounding NPs and gets pulled out and elongated as the crack propagates. It can either remain intact or break during this process.

of the polymer (1.8 nm for PS), N is the number of Kuhn monomers, and ε_{max} is the theoretical maximum strain for a single entangled chain (≈3 for PS).[67] c is a fitting parameter that captures the width of the failure probability distribution. There are two adjustable parameters in this equation (c and τ).

Figure 4c compares the modeling results to the fracture data of PINFs with 27 nm NPs. This molecular strength limiting bridging model captures the overall fracture behavior over a broad range of polymer MWs. τ obtained in PINFs with silane-passivated 27 nm NPs is 169 MPa, much lower than 303 MPa in those with untreated NPs, consistent with a previous report.[60] The deviations of data from this model may be attributed to two reasons. First, this model was derived in nanocomposites with cylindrical pores, and confined polymers are treated cylindrical "fibers". However, the pore geometry in NP packings is very different from that of cylindrical pores and has a broad pore size distribution (narrow necks and wide gaps). Second, the maximum pullout length of confined polymers without chain rupture is assumed to be half the root mean square end-to-end distance ($<R_{ee}^2>^{1/2}$) of polymer chains in the unperturbed state (i.e., $\delta_0 = 1/2 <R_{ee}^2>^{1/2} = 1/2 aN^{1/2}$). Molecular dynamics simulations have shown that polymers in PINFs adopt a more stretched conformation compared to bulk evidenced by a larger $<R_{ee}^2>^{1/2}$.[68] Thus, modifications to the model are needed to more accurately describe the data by accounting for complicated pore geometry and chain conformation change. Nevertheless, this model clearly shows that when PINFs are toughened by confinement-induced molecular bridging, silane passivation impacts the fracture toughness by changing sliding shear stress at polymer−NP interface.

To investigate if G_c of PINFs that are toughened by confinement-induced molecular bridging can be further enhanced by increasing polymer−NP interaction strength, we

https://doi.org/10.1021/acs.macromol.2c01567
Macromolecules 2023, 56, 122−135

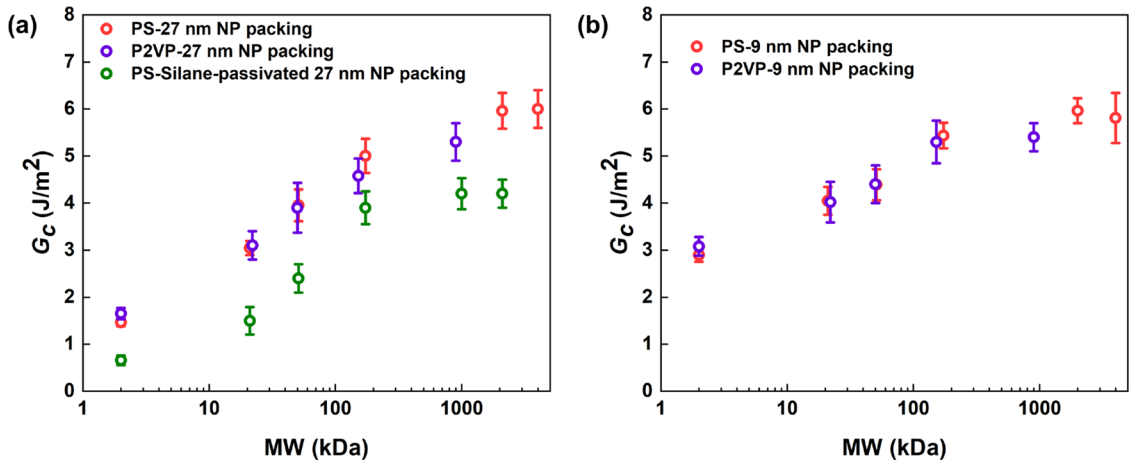

Figure 5. Effect of polymer−NP interaction strength on the fracture toughness of PINFs toughened by confinement-induced molecular bridging: G_c as a function of polymer MW for PINFs made of PS/P2VP and (a) 27 nm NPs and (b) 9 nm NPs. G_c of PINFs made of PS and silane-passivated 27 nm NPs are also included for comparison.

prepare PINFs with P2VP, a polymer known to form strong hydrogen bonding with untreated SiO_2 NPs. Surprisingly, as shown in Figure 5a, 27 nm NP packings infiltrated with PS or P2VP show similar G_c values. Similar results (Figure 5b) and fractured surfaces (Figures S5 and S6) are also observed in 9 nm NP packings, which has larger polymer−NP interfacial area (Figure 2c), in contrast to T_g measurements (Figure 3). We note that the T_g measurements are performed well above RT when PINFs are cooled from melt to glassy state, whereas the fracture toughness measurements are performed at RT when polymers are in a glassy state and adsorbed on NP surfaces. Thus, these two sets of data capture fundamentally different regimes of polymer behavior. In fact, the structure of the adsorbed layer can play a crucial role in determining polymer adhesion and friction.[69−71]

To better understand the results shown in Figure 5, we measure the adhesion between PS/P2VP and SiO_2 by depositing neat polymers on plasma-treated or silane-passivated Si wafers and constructing ADCB specimens, as shown in Figure 6a. In a ADCB specimen, the crack preferentially propagates along the interface between the interlayer and the more compliant beam. The bottom beam where polymer is deposited on is thinner than the top beam, and therefore the crack is driven to the polymer−Si wafer interface, enabling the quantification of adhesion strength between the polymer and the beam. The thickness ratio between bottom beam and top beam (h_2/h_1) is chosen to be ∼0.75, as suggested by a previous study.[72] Highly entangled PS (158 and 173 k) and P2VP (152 k) are used to prevent crack propagation through the polymer layer. Ellipsometry measurements show that there is little-to-no polymer remaining on the bottom beam, confirming that fracture occurs along or very close to the polymer−Si wafer interface. Figure 6b shows the interfacial fracture energy, G_c, of PS or P2VP deposited on plasma-treated or silane-passivated Si wafers (we note that interfacial fracture energy is interchangeably used with interfacial facture toughness or adhesion energy in the literature[28,72,73]). As expected, PS deposited (∼50 nm) on silane-passivated Si wafers shows the lowest G_c. When PS is deposited on plasma-treated Si wafers, G_c increases significantly to ∼12.5 J/m^2, even higher than P2VP prepared at same conditions (∼4.3 J/m^2). A similar trend is observed (i.e., $G_{c,PS\text{-}Si} > G_{c,P2VP\text{-}Si} > G_{c,PS\text{-}silaneSi}$) in thicker films (∼200 nm) with the higher G_c values likely due to higher entanglement density.[23]

SEM and AFM images are taken to examine the crack path and study the morphology of the surfaces after ADCB tests. PS on silane-passivated Si wafers shows featureless surfaces (Figure 6c,d), indicating easy detachment of polymer chains due to weak interfacial interactions (Figure 6i). In contrast, the surface of P2VP film after detaching from hydroxylated Si wafer exhibits increased roughness with evidence of local plastic deformation; the corresponding bottom beam has a few loosely distributed domains of P2VP (Figure 6e,f). The surface of PS film after detaching from hydroxylated Si wafers shows many nanovoids, and the bottom beam has domains with a similar lateral size and height of 2−5 nm (Figures 6g,h and S8). Similar structures are also observed when the thickness of films is increased to ∼200 nm.

We attribute these microscopic textures to the formation of an adsorbed polymer nanolayer, which comprises inner flattened chains and outer loosely adsorbed chains as previously described.[74] Previous reports have shown that the surface coverage of the extracted flattened chains on hydrophilic Si wafers is lower for PS than P2VP.[74,75] Such densely packed flattened chains inhibit the penetration of unadsorbed, free polymer chains and even do not show any adhesion to the chemically identical free polymers on top. In contrast, the loosely adsorbed chains that occupy the rest of the surface can associate strongly with free chains because the tails can entangle and the loops can interdigitate with the free chains (Figure 6j,k).[70,75] Thus, we believe that the domains observed on the bottom beams correspond to the sites where the loosely adsorbed chains form during thermal annealing and are detached from the free chains during the ADCB test. A higher fraction of loosely adsorbed chains in PS films compared to that in P2VP films results in higher G_c. Overall, the ADCB results demonstrate the importance of the structure of polymers at polymer/substrate interfaces on interfacial adhesion.

Irreversible adsorption of polymer chains onto a weakly attractive surface occurs on planar as well as curved surfaces (e.g., NPs).[76−78] Recently, irreversible adsorption of PS around SiO_2 NPs has been directly observed using transmission electron microscopy.[79] Most of polymer chains in 9 and 27 nm NP packing are essentially in the interfacial region, as

https://doi.org/10.1021/acs.macromol.2c01567
Macromolecules 2023, 56, 122−135

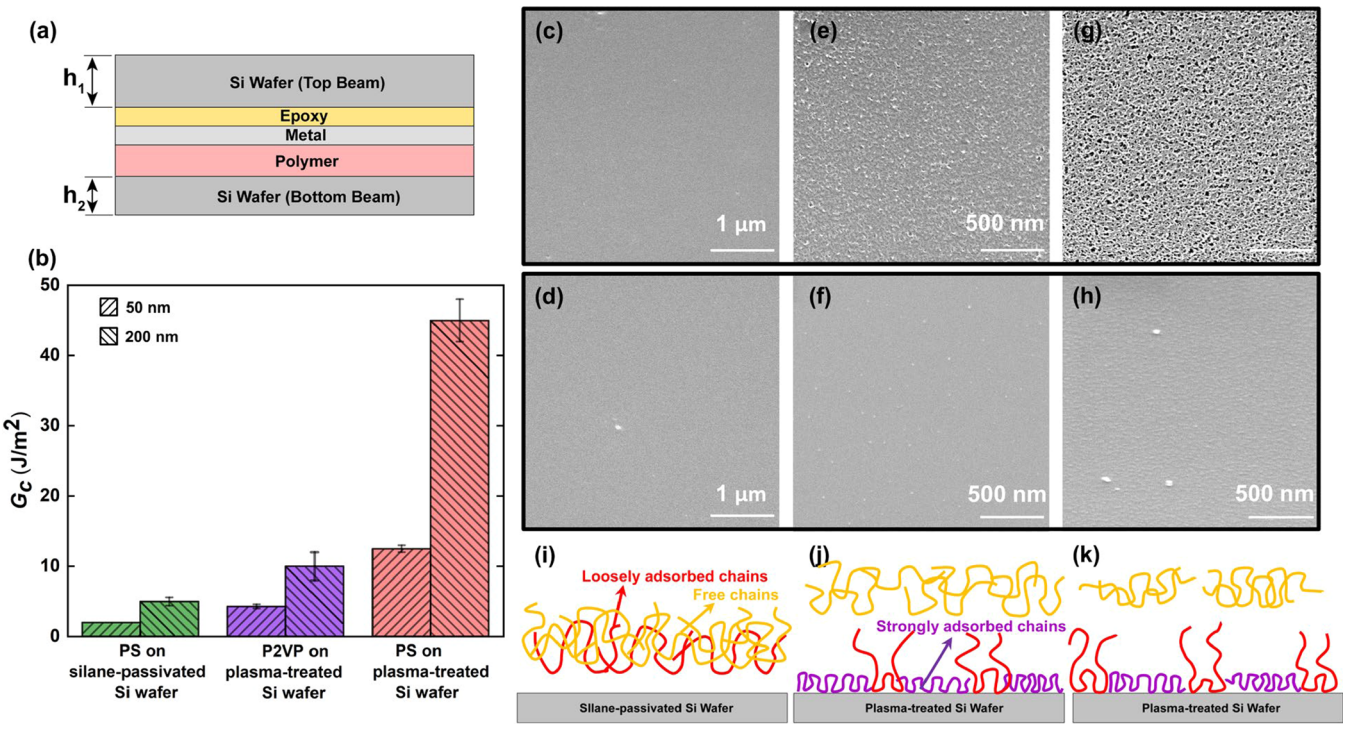

Figure 6. ADCB test for measuring polymer−SiO_2 adhesion: (a) Schematic of the structure of ADCB specimen used to measure polymer−SiO_2 adhesion. The relative thicknesses of each layer are not drawn to scale. (b) Interfacial fracture energy, G_c, of PS/P2VP films on plasma-treated or silane-passivated Si wafers. SEM images of the fractured surfaces of ∼50 nm (c, d) 173 k PS on a silane-passivated Si wafer, (e, f) 152 k P2VP on a plasma-treated Si wafer and (g, h) 173 k PS on a plasma-treated Si wafer. (c), (e), and (g) are taken from the bottom beams where polymers are initially deposited on, while (d), (f), and (h) are taken from the top beams. (i−k) Schematic illustration of the chains left on the bottom beam and on the surface of the top beam after the ADCB test. On silane-passivated Si wafers (i), the polymer chains are loosely adsorbed (red) with low adhesion strength and can be completely detached during the ADCB test. On plasma-treated Si wafers (j and k), some polymer chains are strongly adsorbed with flat conformations (purple) that do not entangle with free chains (yellow). The remaining surface is occupied by loosely adsorbed chains, which can entangle and interdigitate with free chains. Note that the adhesion strength of loosely adsorbed chains on plasma-treated Si wafers is stronger than on silane-passivated Si wafers. Both strongly and loosely adsorbed chains remain on the plasma-treated Si wafers after the ADCB test. The coverage of loosely adsorbed chains is lower in (j) P2VP than (k) PS.

entanglement in these PINFs is significantly reduced or non-existent due to extreme confinement. These chains adopt more stretched conformation compared to bulk and make contact with multiple particles.[80,81] The fracture energy is dissipated by frictional pullout of many individual, strongly adsorbed chains from NP surfaces. We postulate that the contacts between both PS and P2VP chains and untreated SiO_2 NPs act as strong anchoring points during the pullout process. In fact, the interfacial shear stress obtained from the bridging model (303 MPa in untreated and 169 MPa in silane-passivated PINFs) is higher than many reports on polymer−fiber pullout tests (tens of MPa).[60,82] Thus, although the interaction strength between PS-untreated SiO_2 may be weaker than that between P2VP and untreated SiO_2, the adsorbed sites in both interfaces are sufficiently strong to cause high interfacial shear stress and thus result in similar G_c.

3.3.2. PINFs with 79 nm NPs. As NP size increases, polymers become less confined and interchain entanglements within the interstitial voids toughen NP packings.[45] Unlike PINFs with 27 nm NPs, 79 nm NP packings infiltrated with P2VP are in general slightly tougher than those with PS before reaching a similar plateau value of ∼7.3 J/m^2, as shown in Figure 7. For example, 50 k P2VP-79 nm SiO_2 has a G_c of 4.7 J/m^2, 29% higher than 51 k PS-79 nm SiO_2 (3.6 J/m^2). Difference in polymer−NP interaction strength does not account for such an increase because similar G_c values are obtained when the NPs are silane-passivated. For unentangled polymers (e.g., 2 and 21 k), crack propagates by pullout of the short chains from surrounding polymers.[45] With CR ≤ 1 ($CR_{2k,P2VP}$ = 0.11 and $CR_{22k,P2VP}$ = 0.35) and a small interfacial region (∼R_g),[77,83,84] most polymer chains in the pores behave like polymer chains in bulk, and thus the pullout process is

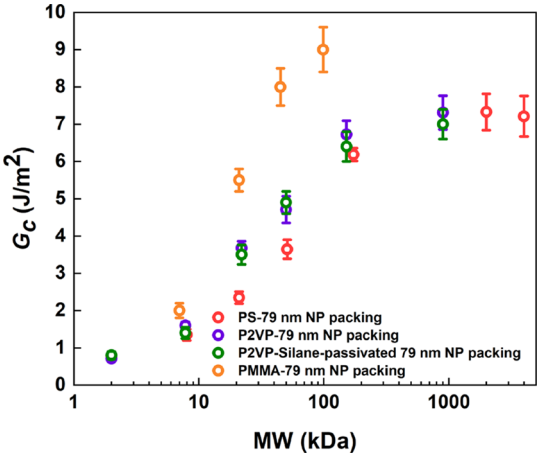

Figure 7. Effect of polymer−NP interaction strength on the fracture toughness of PINFs toughened by polymer entanglement: G_c as a function of polymer MW for PINFs made of 79 nm NPs.

https://doi.org/10.1021/acs.macromol.2c01567
Macromolecules 2023, 56, 122−135

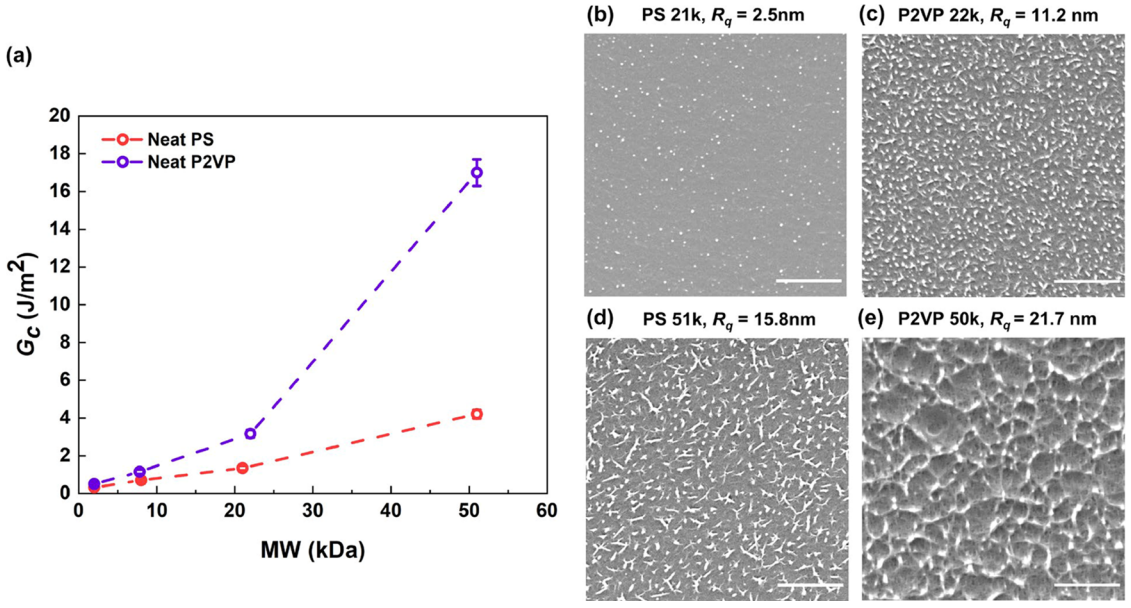

Figure 8. DCB fracture testing of neat polymer films: (a) G_c as a function of polymer MW for neat PS and P2VP films. SEM images of the fractured surfaces of neat PS films with MW of (b) 21 k, (d) 51 k, and neat P2VP films with MW of (c) 22 k and (e) 50 k. All images are taken from the top beams. All scale bars are 500 nm.

unaffected by the change in the interfacial layer. For high MW polymers (e.g., 900 k), even though the chains can form interchain entanglements, the overall entanglement density is greatly reduced compared to bulk.[85−87] In addition, polymer chains adsorbed on the NP surface are found to be elongated and flattened regardless of polymer−NP interactions.[88] The volume pervaded by these chains is smaller than that in the bulk, resulting in further depletion of entanglements near the surface.[84,87,89] Thus, a crack propagates mainly through free, unabsorbed chains and G_c is not strongly influenced by silane passivation of NPs.

Our previous work has shown that the fracture toughness of PINFs approaches that of neat polymers as NP size increases.[45] Thus, the fracture data observed in Figure 7 may be attributed to different fracture properties of PS and P2VP despite their similar chemical structures. To test this hypothesis, the fracture toughness of neat PS and P2VP films is measured, as shown in Figure 8a. While G_c of 2 k P2VP (0.51 ± 0.07 J/m^2) is only slightly higher than 2 k PS (0.32 ± 0.04 J/m^2), the differences between these two polymers become significant as MW increases. The G_c of 8, 22, and 50 k P2VP are 1.6, 2.3, and 4.0 times that of PS of similar MW, respectively. In neat glassy polymers, such as PS and P2VP, fracture mechanism transitions from segment pullout below the critical entanglement M_c ($M_{c,PS}$ = 31,000 g mol^{-1}, $M_{c,P2VP}$ = 36,000 g mol^{-1}) to crazing above M_c.[83,90] In the segmental pullout region, G_c is proportional to monomer friction coefficient ($f_{monomer}$).[91] Thus, we attribute higher G_c in unentangled P2VP to stronger intermolecular forces and a larger $f_{monomer}$. In the crazing region, G_c is equal to the product of critical crack-opening displacement (δ_c) and craze widening stress (σ_{craze}) based on the Dugdale plastic zone model.[92,93] σ_{craze} has been reported to be higher for P2VP (75 ± 5 MPa) than PS (55 ± 5 MPa).[94] The exact values of δ_c are difficult to obtain but are correlated with the feature sizes on the fractured surfaces.[95] SEM and AFM images of the fracture surfaces of PS and P2VP films clearly show that at similar MW, there are noticeable differences in the morphology of fractured films (Figures 8b−e and S9). 21 k PS film shown in Figure 8b shows relatively a smooth surface (R_q = 2.5 nm) with a few small grain-like features, whereas the 22 k P2VP film shown in Figure 8c shows a rougher surface (R_q = 11.2 nm) with a higher density of grain-like features. As MW increases to 51 k, the fractured surface of PS film (Figure 8d) shows a higher roughness (R_q = 15.8 nm) with local plastic deformation. In sharp contrast, 50 k P2VP film (Figure 8e) shows larger-scale plastic deformation with significantly elongated and deformed regions. Larger σ_{craze} and δ_c in P2VP lead to significantly higher G_c of P2VP compared to PS. Due to reduced entanglement density and suppressed load transfer with the presence of NPs,[45] limited plastic deformation occurs during the fracture of PINFs. Thus, P2VP-infiltrated 79 nm NP films are slightly tougher than those with PS and the overall G_c values are lower than neat polymer films. We further confirm the dependence of G_c of PINFs on the fracture properties of infiltrated polymers by testing PMMA-infiltrated 79 nm films. PMMA is known to have a lower M_c ($M_{c,PS}$ = 18,400 g mol^{-1}) and a higher σ_{craze} (100 ± 10 MPa).[94,96] As shown in Figure 7, at a similar MW (e.g., 8, 21, and 45 k), PMMA-infiltrated NP films show larger G_c compared to those with PS or P2VP.

4. CONCLUSIONS

In summary, we investigate the role of polymer−NP interaction strength on the fracture toughness of a new class of highly loaded PNCFs prepared via CaRI of polymer into disordered packing of NPs. We tune polymer−NP interaction strength by using SiO_2 NPs with hydroxyl or trimethylsilyl groups and two polymers (PS and P2VP) that are known to have different interaction strengths with NPs. When PINFs are toughened via confinement-induced molecular bridging, the fracture toughness is affected by the interfacial shear stress evident in silane-passivated samples. PS and P2VP show no distinguishable difference, as both polymers can strongly adsorb onto untreated NPs and the contact sites act as strong anchoring points during the pullout process. In contrast, the fracture toughness of PINFs with large NPs is more dependent

https://doi.org/10.1021/acs.macromol.2c01567
Macromolecules 2023, 56, 122−135

on the fracture properties of polymers than on the polymer−NP interaction strength. Our work offers insights into how polymer−NP interactions alter the fracture behavior of confined polymers and provide guidelines for the design of mechanically robust PINFs as well as other highly loaded PNCFs.

■ ASSOCIATED CONTENT

Supporting Information

The Supporting Information is available free of charge at https://pubs.acs.org/doi/10.1021/acs.macromol.2c01567.

Surface energies of probe liquid, polymer, and SiO_2 NPs; detailed information about NP size, pore size, porosity of SiO_2 NP films, BET surface area, pore diameter, and pore volume of bulk SiO_2 NP packings; modulus of uninfiltrated (neat) and PS-infiltrated NP films; percent of pores filled with condensed water for untreated and silane-passivated 79 nm SiO_2 NP films upon exposure to water vapor; dewetting of PS on silane-passivated NP films; in situ ellipsometry data of polymer/NP bilayer films annealed at 443 K; SEM images of the fracture surfaces of PINFs; SEM and AFM images of a Si wafer where a 50 nm thick 173 k PS layer is initially deposited on and detached after the ADCB test; AFM images of fractured polymer films; effect of polymer−nanoparticle interaction strength on infiltration dynamics; T_g extraction from spectroscopic ellipsometry data; effect of confinement on the modulus of PINFs; confinement-induced molecular bridging model; and keys to achieving intrinsic fracture toughness measurement of PINFs (PDF)

■ AUTHOR INFORMATION

Corresponding Authors

Kevin T. Turner − *Department of Mechanical Engineering and Applied Mechanics and Department of Materials Science and Engineering, University of Pennsylvania, Philadelphia, Pennsylvania 19104, United States;* orcid.org/0000-0003-4963-4568; Email: kturner@seas.upenn.edu

Daeyeon Lee − *Department of Chemical and Biomolecular Engineering, University of Pennsylvania, Philadelphia, Pennsylvania 19104, United States;* orcid.org/0000-0001-6679-290X; Email: daeyeon@seas.upenn.edu

Author

Yiwei Qiang − *Department of Materials Science and Engineering, University of Pennsylvania, Philadelphia, Pennsylvania 19104, United States;* orcid.org/0000-0001-6839-2993

Complete contact information is available at: https://pubs.acs.org/10.1021/acs.macromol.2c01567

Author Contributions

Y.Q., K.T.T., and D.L. conceived the experiments. Y.Q. conducted the experiments. Y.Q., K.T.T., and D.L. analyzed the experimental results. K.T.T. and D.L. supervised the work. The manuscript was written through contributions of all authors. All authors have given approval to the final version of the manuscript.

Notes

The authors declare no competing financial interest.

■ ACKNOWLEDGMENTS

This work was supported by National Science Foundation via MRSEC DMR-1720530 and CMMI-1662695. Facilities support was provided by the Singh Center for Nanotechnology, part of the National Nanotechnology Coordinated Infrastructure Program, which is supported by the National Science Foundation grant NNCI-2025608. We thank Nissan Chemical America Corp. for supplying the Snowtex ST-YL and ST-ZL SiO_2 NP suspensions. We also thank Yueli Chen for her help with the glass transition temperature measurements.

■ REFERENCES

(1) Alonso-Redondo, E.; Belliard, L.; Rolle, K.; Graczykowski, B.; Tremel, W.; Djafari-Rouhani, B.; Fytas, G. Robustness of Elastic Properties in Polymer Nanocomposite Films Examined over the Full Volume Fraction Range. *Sci. Rep.* **2018**, *8*, 16986.

(2) Zou, H.; Wu, S.; Shen, J. Polymer/Silica Nanocomposites: Preparation, Characterization, Propertles, and Applications. *Chem. Rev.* **2008**, *108*, 3893−3957.

(3) Kumar, S. K.; Benicewicz, B. C.; Vaia, R. A.; Winey, K. I. 50th Anniversary Perspective: Are Polymer Nanocomposites Practical for Applications? *Macromolecules* **2017**, *50*, 714−731.

(4) Harito, C.; Bavykin, D. V.; Yuliarto, B.; Dipojono, H. K.; Walsh, F. C. Polymer Nanocomposites Having a High Filler Content: Synthesis, Structures, Properties, and Applications. *Nanoscale* **2019**, *11*, 4653−4682.

(5) Suresh, K.; Chowdhury, A.; Kumar, S. K.; Kumaraswamy, G. Critical Role of Processing on the Mechanical Properties of Cross-Linked Highly Loaded Nanocomposites. *Macromolecules* **2019**, *52*, 5955−5962.

(6) Merkel, T. C.; Freeman, B. D.; Spontak, R. J.; He, Z.; Pinnau, I.; Meakin, P.; Hill, A. J. Ultrapermeable, Reverse-Selective Nanocomposite Membranes. *Science* **2002**, *296*, 519−522.

(7) Freeman, B. D. Basis of Permeability/Selectivity Tradeoff Relations in Polymeric Gas Separation Membranes. *Macromolecules* **1999**, *32*, 375−380.

(8) Hoffmann, R.; Baric, V.; Naatz, H.; Schopf, S. O.; Mädler, L.; Hartwig, A. Inverse Nanocomposites Based on Indium Tin Oxide for Display Applications: Improved Electrical Conductivity via Polymer Addition. *ACS Appl. Nano Mater.* **2019**, *2*, 2273−2282.

(9) Zhu, H.; Li, Y.; Fang, Z.; Xu, J.; Cao, F.; Wan, J.; Preston, C.; Yang, B.; Hu, L. Highly Thermally Conductive Papers with Percolative Layered Boron Nitride Nanosheets. *ACS Nano* **2014**, *8*, 3606−3613.

(10) Zhang, X.; Shi, C.; Liu, E.; Zhao, N.; He, C. Effect of Interface Structure on the Mechanical Properties of Graphene Nanosheets Reinforced Copper Matrix Composites. *ACS Appl. Mater. Interfaces* **2018**, *10*, 37586−37601.

(11) Wagner, H. D.; Vaia, R. A. Nanocomposites: Issues at the Interface. *Mater. Today* **2004**, *7*, 38−42.

(12) Chan, K. S.; Lee, Y. D.; Nicolella, D. P.; Furman, B. R.; Wellinghoff, S.; Rawls, R. Improving Fracture Toughness of Dental Nanocomposites by Interface Engineering and Micromechanics. *Eng. Fract. Mech.* **2007**, *74*, 1857−1871.

(13) Wang, Y.; Yang, C.; Pei, Q. X.; Zhang, Y. Some Aspects of Thermal Transport across the Interface between Graphene and Epoxy in Nanocomposites. *ACS Appl. Mater. Interfaces* **2016**, *8*, 8272−8279.

(14) Luo, H.; Zhou, X.; Ellingford, C.; Zhang, Y.; Chen, S.; Zhou, K.; Zhang, D.; Bowen, C. R.; Wan, C. Interface Design for High Energy Density Polymer Nanocomposites. *Chem. Soc. Rev.* **2019**, *48*, 4424−4465.

(15) Bailey, E. J.; Winey, K. I. Dynamics of Polymer Segments, Polymer Chains, and Nanoparticles in Polymer Nanocomposite Melts: A Review. *Prog. Polym. Sci.* **2020**, *105*, No. 101242.

(16) Qin, X.; Xia, W.; Sinko, R.; Keten, S. Tuning Glass Transition in Polymer Nanocomposites with Functionalized Cellulose Nanocrystals through Nanoconfinement. *Nano Lett.* **2015**, *15*, 6738−6744.

(17) Ma, H.; Lionti, K.; Magbitang, T. P.; Gaskins, J.; Hopkins, P. E.; Huxtable, S. T.; Tian, Z. Pore-Confined Polymers Enhance the Thermal Conductivity of Polymer Nanocomposites. *ACS Macro Lett.* **2022**, *11*, 116−120.
(18) Nimmi Das, A.; Begam, N.; Ibrahim, M.; Chandran, S.; Padmanabhan, V.; Sprung, M.; Basu, J. K. Viscosity and Fragility of Confined Polymer Nanocomposites: A Tale of Two Interfaces. *Nanoscale* **2019**, *11*, 8546−8553.
(19) Schilling, T.; Habel, C.; Rosenfeldt, S.; Rohrl, M.; Breu, J. Impact of Ultraconfinement on Composite Barriers. *ACS Appl. Polym. Mater.* **2020**, *2*, 3010−3015.
(20) Bay, R. K.; Zarybnicka, K.; Jančář, J.; Crosby, A. J. Mechanical Properties of Ultrathin Polymer Nanocomposites. *ACS Appl. Polym. Mater.* **2020**, *2*, 2220−2227.
(21) Genix, A. C.; Bocharova, V.; Kisliuk, A.; Carroll, B.; Zhao, S.; Oberdisse, J.; Sokolov, A. P. Enhancing the Mechanical Properties of Glassy Nanocomposites by Tuning Polymer Molecular Weight. *ACS Appl. Mater. Interfaces* **2018**, *10*, 33601−33610.
(22) Shao, C.; Keten, S. Stiffness Enhancement in Nacre-Inspired Nanocomposites Due to Nanoconfinement. *Sci. Rep.* **2015**, *5*, 16452.
(23) Zhang, S.; Koizumi, M.; Cao, Z.; Mao, K. S.; Qian, Z.; Galuska, L. A.; Jin, L.; Gu, X. Directly Probing the Fracture Behavior of Ultrathin Polymeric Films. *ACS Polym. Au* **2021**, *1*, 16−29.
(24) Lee, J. H.; Chung, J. Y.; Stafford, C. M. Effect of Confinement on Stiffness and Fracture of Thin Amorphous Polymer Films. *ACS Macro Lett.* **2012**, *1*, 122−126.
(25) Matsuda, Y.; Yang, J.; Fitzgibbons, T.; Rao, Y. Glasslike Polymer Nanocomposite Coating via High Loading of Mixed-Size Nanoparticles. *ACS Appl. Polym. Mater.* **2022**, *4*, 672−681.
(26) Dreyer, A.; Feld, A.; Kornowski, A.; Yilmaz, E. D.; Noei, H.; Meyer, A.; Krekeler, T.; Jiao, C.; Stierle, A.; Abetz, V.; Weller, H.; Schneider, G. A. Organically Linked Iron Oxide Nanoparticle Supercrystals with Exceptional Isotropic Mechanical Properties. *Nat. Mater.* **2016**, *15*, 522−528.
(27) Santagiuliana, G.; Picot, O. T.; Crespo, M.; Porwal, H.; Zhang, H.; Li, Y.; Rubini, L.; Colonna, S.; Fina, A.; Barbieri, E.; Spoelstra, A. B.; Mirabello, G.; Patterson, J. P.; Botto, L.; Pugno, N. M.; Peijs, T.; Bilotti, E. Breaking the Nanoparticle Loading-Dispersion Dichotomy in Polymer Nanocomposites with the Art of Croissant-Making. *ACS Nano* **2018**, *12*, 9040−9050.
(28) Anderson, T. L.. *Fracture Mechanics: Fundamentals and Applications*; CRC Press: Boca Raton, 2005.
(29) Venkatesh, R. B.; Manohar, N.; Qiang, Y.; Wang, H.; Tran, H. H.; Kim, B. Q.; Neuman, A.; Ren, T.; Fakhraai, Z.; Riggleman, R. A.; Stebe, K. J.; Turner, K.; Lee, D. Polymer-Infiltrated Nanoparticle Films Using Capillarity-Based Techniques: Toward Multifunctional Coatings and Membranes. *Annu. Rev. Chem. Biomol. Eng.* **2021**, *12*, 411−437.
(30) Wang, H.; Hor, J. L.; Zhang, Y.; Liu, T.; Lee, D.; Fakhraai, Z. Dramatic Increase in Polymer Glass Transition Temperature under Extreme Nanoconfinement in Weakly Interacting Nanoparticle Films. *ACS Nano* **2018**, *12*, 5580−5587.
(31) Hor, J. L.; Wang, H.; Fakhraai, Z.; Lee, D. Effects of Polymer-Nanoparticle Interactions on the Viscosity of Unentangled Polymers under Extreme Nanoconfinement during Capillary Rise Infiltration. *Soft Matter* **2018**, *14*, 2438−2446.
(32) Natarajan, B.; Li, Y.; Deng, H.; Brinson, L. C.; Schadler, L. S. Effect of Interfacial Energetics on Dispersion and Glass Transition Temperature in Polymer Nanocomposites. *Macromolecules* **2013**, *46*, 2833−2841.
(33) Buitrago, C. F.; Pressly, J. F.; Yang, A. S.; Gordon, P. A.; Riggleman, R. A.; Natarajan, B.; Winey, K. I. Creep Attenuation in Glassy Polymer Nanocomposites with Variable Polymer-Nanoparticle Interactions. *Soft Matter* **2020**, *16*, 8912−8924.
(34) Huang, Y. R.; Jiang, Y.; Hor, J. L.; Gupta, R.; Zhang, L.; Stebe, K. J.; Feng, G.; Turner, K. T.; Lee, D. Polymer Nanocomposite Films with Extremely High Nanoparticle Loadings via Capillary Rise Infiltration (CaRI). *Nanoscale* **2015**, *7*, 798−805.
(35) Manohar, N. Solvent-Driven Infiltration of Polymer (SIP) Into Nanoparticle Packings; University of Pennsylvania ProQuest Dissertations Publishing, 2020.
(36) Venkatesh, R. B.; Han, S. H.; Lee, D. Patterning Polymer-Filled Nanoparticle Films via Leaching-Enabled Capillary Rise Infiltration (LeCaRI). *Nanoscale Horiz.* **2019**, *4*, 933−939.
(37) Qiang, Y.; Manohar, N.; Stebe, K. J.; Lee, D. Polymer Blend-Filled Nanoparticle Films: Via Monomer-Driven Infiltration of Polymer and Photopolymerization. *Mol. Syst. Des. Eng.* **2018**, *3*, 96−102.
(38) Qiang, Y.; Turner, K. T.; Lee, D. Polymer-Infiltrated Nanoplatelet Films with Nacre-like Structure: Via Flow Coating and Capillary Rise Infiltration (CaRI). *Nanoscale* **2021**, *13*, 5545−5556.
(39) Kim, B. Q.; Qiang, Y.; Turner, K. T.; Choi, S. Q.; Lee, D. Heterostructured Polymer-Infiltrated Nanoparticle Films with Cavities via Capillary Rise Infiltration. *Adv. Mater. Interfaces* **2020**, *8*, No. 2001421.
(40) Wang, H.; Qiang, Y.; Shamsabadi, A. A.; Mazumder, P.; Turner, K. T.; Lee, D.; Fakhraai, Z. Thermal Degradation of Polystyrene under Extreme Nanoconfinement. *ACS Macro Lett.* **2019**, *8*, 1413−1418.
(41) Hor, J. L.; Wang, H.; Fakhraai, Z.; Lee, D. Effect of Physical Nanoconfinement on the Viscosity of Unentangled Polymers during Capillary Rise Infiltration. *Macromolecules* **2018**, *51*, 5069−5078.
(42) Donovan, B. F.; Warzoha, R. J.; Venkatesh, R. B.; Vu, N. T.; Wallen, J.; Lee, D. Elimination of Extreme Boundary Scattering via Polymer Thermal Bridging in Silica Nanoparticle Packings: Implications for Thermal Management. *ACS Appl. Nano Mater.* **2019**, *2*, 6662−6669.
(43) Wang, H. *Tuning the Properties of Soft Materials through Extreme Nanoconfinement*; University of Pennsylvania ProQuest Dissertations Publishing, 2020.
(44) Venkatesh, R. B.; Zhang, T.; Manohar, N.; Stebe, K. J.; Riggleman, R. A.; Lee, D. Effect of Polymer-Nanoparticle Interactions on Solvent-Driven Infiltration of Polymer (SIP) into Nanoparticle Packings: A Molecular Dynamics Study. *Mol. Syst. Des. Eng.* **2020**, *5*, 666−674.
(45) Qiang, Y.; Pande, S. S.; Lee, D.; Turner, K. T. The Interplay of Polymer Bridging and Entanglement in Toughening Polymer-Infiltrated Nanoparticle Films. *ACS Nano* **2022**, *16*, 6372−6381.
(46) Venkatesh, R. B.; Lee, D. Conflicting Effects of Extreme Nanoconfinement on the Translational and Segmental Motion of Entangled Polymers. *Macromolecules* **2022**, *55*, 4492−4501.
(47) Kanninen, M. F. An Augmented Double Cantilever Beam Model for Studying Crack Propagation and Arrest. *Int. J. Fract.* **1973**, *9*, 83−92.
(48) Stavig, M. E.; Jaramillo, R.; Larkin, E. C.; Dugger, J. W.; Reedy, E. D. *Asymmetric Double Cantilever Beam Test to Measure the Toughness of an Alumina/Epoxy Interface*; 2019.
(49) Kamer, A.; Larson-Smith, K.; Pingree, L. S. C.; Dauskardt, R. H. Adhesion and Degradation of Hard Coatings on Poly (Methyl Methacrylate) Substrates. *Thin Solid Films* **2011**, *519*, 1907−1913.
(50) Oliver, W. C.; Pharr, G. M. Measurement of Hardness and Elastic Modulus by Instrumented Indentation: Advances in Understanding and Refinements to Methodology W.C. *J. Mater. Res.* **2004**, *19*, 3−20.
(51) Ralf, S.; Karin, J.; Ralf, B. Polystyrene Nanodroplets. *J. Phys. Condens. Matter* **2001**, *13*, 4915.
(52) Shin, K.; Obukhov, S.; Chen, J. T.; Huh, J.; Hwang, Y.; Mok, S.; Dobriyal, P.; Thiyagarajan, P.; Russell, T. P. Enhanced Mobility of Confined Polymers. *Nat. Mater.* **2007**, *6*, 961−965.
(53) Holt, A. P.; Griffin, P. J.; Bocharova, V.; Agapov, A. L.; Imel, A. E.; Dadmun, M. D.; Sangoro, J. R.; Sokolov, A. P. Dynamics at the Polymer/Nanoparticle Interface in Poly(2-Vinylpyridine)/ Silica Nanocomposites. *Macromolecules* **2014**, *47*, 1837−1843.
(54) Wei, T.; Torkelson, J. M. Molecular Weight Dependence of the Glass Transition Temperature (Tg)-Confinement Effect in Well-Dispersed Poly(2-Vinyl Pyridine)-Silica Nanocomposites: Compar-

https://doi.org/10.1021/acs.macromol.2c01567
Macromolecules 2023, 56, 122−135

ison of Interfacial Layer Tgand Matrix Tg. *Macromolecules* **2020**, *53*, 8725−8736.
(55) Voylov, D. N.; Holt, A. P.; Doughty, B.; Bocharova, V.; Meyer, H. M.; Cheng, S.; Martin, H.; Dadmun, M.; Kisliuk, A.; Sokolov, A. P. Unraveling the Molecular Weight Dependence of Interfacial Interactions in Poly(2-Vinylpyridine)/Silica Nanocomposites. *ACS Macro Lett.* **2017**, *6*, 68−72.
(56) Stöckelhuber, K.; Das, A.; Jurk, R.; Heinrich, G. Contribution of Physico-Chemical Properties of Interfaces on Dispersibility, Adhesion and Flocculation of Filler Particles in Rubber. *Polymer* **2010**, *51*, 1954−1963.
(57) Mortezaei, M.; Famili, M. H. N.; Kokabi, M. The Role of Interfacial Interactions on the Glass-Transition and Viscoelastic Properties of Silica/Polystyrene Nanocomposite. *Compos. Sci. Technol.* **2011**, *71*, 1039−1045.
(58) Robert, N. Surface Roughness and Contact Angle. *J. Phys. Chem.* **1949**, *53*, 1466−1467.
(59) Sindorf, D. W.; Maciel, G. E. Cross-Polarization/Magic-Angle-Spinning Silicon-29 Nuclear Magnetic Resonance Study of Silica Gel Using Trimethylsilane Bonding as a Probe of Surface Geometry and Reactivity. *J. Phys. Chem.* **1982**, *86*, 5208−5219.
(60) Wang, C.; Isaacson, S. G.; Wang, Y.; Lionti, K.; Volksen, W.; Magbitang, T. P.; Chowdhury, M.; Priestley, R. D.; Dubois, G.; Dauskardt, R. H. Surface Chemical Functionalization to Achieve Extreme Levels of Molecular Confinement in Hybrid Nanocomposites. *Adv. Funct. Mater.* **2019**, *29*, No. 1903132.
(61) Zhao, X. S.; Lu, G. Q. Modification of MCM-41 by Surface Silylation with Trimethylchlorosilane and Adsorption Study. *J. Phys. Chem. B* **1998**, *102*, 1556−1561.
(62) Bertei, A.; Nucci, B.; Nicolella, C. Effective Transport Properties in Random Packings of Spheres and Agglomerates. *Chem. Eng. Trans.* **2013**, *32*, 1531−1536.
(63) Zhang, D.; Xu, Y.; Feng, G.; Huang, Y.-R.; Lee, D. Comparing Sintering and Atomic Layer Deposition as Methods to Mechanically Reinforce Nanocolloidal Crystals. *J. Mater. Res.* **2015**, *30*, 3717−3727.
(64) Rittigstein, P.; Torkelson, J. M. Polymer−Nanoparticle Interfacial Interactions in Polymer Nanocomposites: Confinement Effects on Glass Transition Temperature and Suppression of Physical Aging. *J. Polym. Sci. B Polym. Phys.* **2006**, *44*, 2935−2943.
(65) Gibbs, J.; DiMarzio, E. A. Nature of the Glass Transition and the Glassy State. *J. Chem. Phys.* **1958**, *28*, 373−383.
(66) Isaacson, S. G.; Lionti, K.; Volksen, W.; Magbitang, T. P.; Matsuda, Y.; Dauskardt, R. H.; Dubois, G. Fundamental Limits of Material Toughening in Molecularly Confined Polymers. *Nat. Mater.* **2016**, *15*, 294−298.
(67) Kramer, E. J. Microscopic and Molecular Fundamentals of Crazing. In *Crazing in polymers*; Springer: Berlin, Heidelberg, 1983; pp. 1−56.
(68) Lin, E. Y.; Frischknecht, A. L.; Riggleman, R. A. Chain and Segmental Dynamics in Polymer−Nanoparticle Composites with High Nanoparticle Loading. *Macromolecules* **2021**, *54*, 5335−5343.
(69) Raos, G.; Zappone, B. Polymer Adhesion: Seeking New Solutions for an Old Problem. *Macromolecules* **2021**, *54*, 10617−10644.
(70) Jiang, N.; Sen, M.; Zeng, W.; Chen, Z.; Cheung, J. M.; Morimitsu, Y.; Endoh, M. K.; Koga, T.; Fukuto, M.; Yuan, G.; Satija, S. K.; Carrillo, J. M. Y.; Sumpter, B. G. Structure-Induced Switching of Interpolymer Adhesion at a Solid-Polymer Melt Interface. *Soft Matter* **2018**, *14*, 1108−1119.
(71) Léger, L.; Raphaël, E.; Hervet, H. Surface-Anchored Polymer Chains: Their Role in Adhesion and Friction. In *Polymers in Confined Environments*; Springer: Berlin, Heidelberg, 1999; Vol. *138*, pp. 186−225.
(72) Smith, J. W. M.; Kramer, E. J.; Xiao, F.; Hui, C. Y.; Reichert, W.; Brown, H. R. Measurement of the Fracture Toughness of Polymer-Non-Polymer Interfaces. *J. Mater. Sci.* **1993**, *28*, 4234−4244.
(73) Lee, I.; Kim, S.; Yun, J.; Park, I.; Kim, T. S. Interfacial Toughening of Solution Processed Ag Nanoparticle Thin Films by Organic Residuals. *Nanotechnology* **2012**, *23*, No. 485704.
(74) Jiang, N.; Shang, J.; Di, X.; Endoh, M. K.; Koga, T. Formation Mechanism of High-Density, Flattened Polymer Nanolayers Adsorbed on Planar Solids. *Macromolecules* **2014**, *47*, 2682−2689.
(75) Jiang, N.; Wang, J.; Di, X.; Cheung, J.; Zeng, W.; Endoh, M. K.; Koga, T.; Satija, S. K. Nanoscale Adsorbed Structures as a Robust Approach for Tailoring Polymer Film Stability. *Soft Matter* **2016**, *12*, 1801−1809.
(76) Fujii, Y.; Yang, Z.; Leach, J.; Atarashi, H.; Tanaka, K.; Tsui, O. K. C. Affinity of Polystyrene Films to Hydrogen-Passivated Silicon and Its Relevance to the Tg of the Films. *Macromolecules* **2009**, *42*, 7418−7422.
(77) Jouault, N.; Moll, J. F.; Meng, D.; Windsor, K.; Ramcharan, S.; Kearney, C.; Kumar, S. K. Bound Polymer Layer in Nanocomposites. *ACS Macro Lett.* **2013**, *2*, 371−374.
(78) Yavitt, B. M.; Salatto, D.; Zhou, Y.; Huang, Z.; Endoh, M.; Wiegart, L.; Bocharova, V.; Ribbe, A. E.; Sokolov, A. P.; Schweizer, K. S.; Koga, T. Collective Nanoparticle Dynamics Associated with Bridging Network Formation in Model Polymer Nanocomposites. *ACS Nano* **2021**, *15*, 11501−11513.
(79) Randazzo, K.; Bartkiewicz, M.; Graczykowski, B.; Cangialosi, D.; Fytas, G.; Zuo, B.; Priestley, R. D. Direct Visualization and Characterization of Interfacially Adsorbed Polymer atop Nanoparticles and within Nanocomposites. *Macromolecules* **2021**, *54*, 10224−10234.
(80) Jiang, Y.; Hor, J. L.; Lee, D.; Turner, K. T. Toughening Nanoparticle Films via Polymer Infiltration and Confinement. *ACS Appl. Mater. Interfaces* **2018**, *10*, 44011−44017.
(81) Lin, E. Y.; Frischknecht, A. L.; Riggleman, R. A. Origin of Mechanical Enhancement in Polymer Nanoparticle (NP) Composites with Ultrahigh NP Loading. *Macromolecules* **2020**, *53*, 2976−2982.
(82) Ozkan, T.; Chen, Q.; Chasiotis, I. Interfacial Strength and Fracture Energy of Individual Carbon Nanofibers in Epoxy Matrix as a Function of Surface Conditions. *Compos. Sci. Technol.* **2012**, *72*, 965−975.
(83) Griffin, P. J.; Bocharova, V.; Middleton, L. R.; Composto, R. J.; Clarke, N.; Schweizer, K. S.; Winey, K. I. Influence of the Bound Polymer Layer on Nanoparticle Diffusion in Polymer Melts. *ACS Macro Lett.* **2016**, *5*, 1141−1145.
(84) Weir, M. P.; Johnson, D. W.; Boothroyd, S. C.; Savage, R. C.; Thompson, R. L.; King, S. M.; Rogers, S. E.; Coleman, K. S.; Clarke, N. Distortion of Chain Conformation and Reduced Entanglement in Polymer-Graphene Oxide Nanocomposites. *ACS Macro Lett.* **2016**, *5*, 430−434.
(85) Li, Y.; Kröger, M.; Liu, W. K. Nanoparticle Effect on the Dynamics of Polymer Chains and Their Entanglement Network. *Phys. Rev. Lett.* **2012**, *109*, No. 118001.
(86) Schneider, G. J.; Nusser, K.; Willner, L.; Falus, P.; Richter, D. Dynamics of Entangled Chains in Polymer Nanocomposites. *Macromolecules* **2011**, *44*, 5857−5860.
(87) Vladkov, M.; Barrat, J. L. Local Dynamics and Primitive Path Analysis for a Model Polymer Melt near a Surface. *Macromolecules* **2007**, *40*, 3797−3804.
(88) Starr, F. W.; Schrøder, T. B.; Glotzer, S. C. Molecular Dynamics Simulation of a Polymer Melt with a Nanoscopic Particle. *Macromolecules* **2002**, *35*, 4481−4492.
(89) Hugh, R.; Russell, T. P. Entanglements at Polymer Surfaces and Interfaces. *J. Am. Chem. Soc.* **1996**, *29*, 798−800.
(90) Wool, R. P. Rigidity Percolation Model of Polymer Fracture. *J. Polym. Sci. B Polym. Phys.* **2005**, *43*, 168−183.
(91) Washiyama, J.; Kramer, E. J.; Creton, C. F.; Hui, C. Y. Chain Pullout Fracture of Polymer Interfaces. *Macromolecules* **1994**, *27*, 2019−2024.
(92) Kramer, E. J.; Norton, L. J.; Dai, C. A.; Sha, Y.; Hui, C. Y. Strengthening Polymer Interfaces. *Faraday Discuss.* **1994**, *98*, 31−46.
(93) Pitman, G. L.; Ward, I. M. Effect of Molecular Weight on Craze Shape and Fracture Toughness in Polycarbonate. *Polymer* **1979**, *20*, 895−902.

https://doi.org/10.1021/acs.macromol.2c01567
Macromolecules 2023, 56, 122−135

(94) Creton, C.; Kramer, E. J.; Hui, C. Y.; Brown, H. R. Failure Mechanisms of Polymer Interfaces Reinforced with Block Copolymers. *Macromolecules* **1992**, *25*, 3075−3088.
(95) Bruner, C.; Novoa, F.; Dupont, S.; Dauskardt, R. Decohesion Kinetics in Polymer Organic Solar Cells. *ACS Appl. Mater. Interfaces* **2014**, *6*, 21474−21483.
(96) Wool, R. P. Polymer Entanglements. *Macromolecules* **1993**, *26*, 1564−1569.

https://doi.org/10.1021/acs.macromol.2c01567
Macromolecules 2023, 56, 122−135